Computers & Fluids 66 (2012) 52–62

Contents lists available at SciVerse ScienceDirect

Computers & Fluids

journal homepage: www.elsevier.com/locate/compfluid

Measurement and simulation of a droplet population in a turbulent flow field

Róbert Bordás [a,1], Volker John [b,c], Ellen Schmeyer [b,2], Dominique Thévenin [a,*]

[a] Lab. of Fluid Dynamics & Technical Flows, University of Magdeburg "Otto von Guericke", Magdeburg, Germany
[b] Weierstrass Institute for Applied Analysis and Stochastics, Leibniz Institute in Forschungsverbund Berlin e.V., Berlin, Germany
[c] Department of Mathematics and Computer Science, Free University of Berlin, Berlin, Germany

ARTICLE INFO

Article history:
Received 14 March 2011
Received in revised form 24 April 2012
Accepted 7 May 2012
Available online 30 May 2012

Keywords:
Two-phase turbulent flow
Disperse droplet population
Non-intrusive measurements
Population balance systems
Variational multiscale method

ABSTRACT

The interaction of a disperse droplet population (spray) in a turbulent flow field has been investigated by combining wind tunnel experiments with simulations based on a population balance system. The behavior of the droplets is modeled numerically by a population balance equation. Velocities of the air and of the droplets are determined by non-intrusive measurements. A direct discretization of the 4D equation for the droplet size distribution is used in the simulations. Important components of the numerical algorithm are a variational multiscale method for turbulence modeling, stabilized finite difference schemes for the 4D equation and a pre-processing approach to evaluate the collision integrals. The simulations of this system accurately predict the modifications of the droplet size distribution from the inlet to the outlet of the measurement section. Since the employed configuration is simple and considering that all measurement data are freely available thanks to an internet-based repository, the considered experiment is proposed as a benchmark problem for the simulation of disperse two-phase turbulent flows.

1. Introduction

In this paper detailed numerical simulations of systematic experimental studies concerning droplet populations interacting with a turbulent flow are presented. Such investigations are important to characterize modifications in the Droplet Size Distribution (DSD) resulting from droplet/droplet interactions induced by turbulent structures.

Water droplets with an initial diameter up to 50 μm are injected into a Göttingen-type wind tunnel with a closed test section. Velocities of both phases (air and droplets) are carefully determined by means of non-intrusive measurement techniques. In this way, suitable time-averaged boundary conditions and data are available to validate corresponding numerical simulations.

All measurement data are collected in an online database accessible at http://www.ovgu.de/isut/lss/metstroem. The raw measurement results are further post-processed, so that all required data are in a suitable form for comparisons and validation.

The behavior of the droplet population is modeled by means of a population balance system, consisting of the Navier–Stokes equations describing the air flow together with an additional equation for the DSD. In this last equation, the transport, growth, and coalescence of droplets is taken into account. The DSD describes the spatial evolution of the diameter of the droplets, the so-called internal coordinate, such that the equation for the DSD is finally defined in a 4D domain.

Population balance systems can be applied for modeling many processes in engineering and nature, like precipitation and crystallization processes, or rain formation. The development of accurate and efficient numerical methods for such simulations is an active field of research. Several suitable approaches have been proposed in the literature. In particular, moment-based methods like the quadrature method of moments (QMOM) [34], in which the equation in the 4D domain is replaced by a system of equations for the moments defined in the 3D flow domain, appears promising. A possible extension of QMOM is the direct quadrature method of moments (DQMOM) [33]. Further, operator splitting techniques have been studied recently [8], projecting the solution of the 4D problem onto the solution of a 1D problem followed by the solution of a 3D problem. Moment-based approaches and operator splitting schemes are beneficial, since the solution of the 4D equation is not needed any more. On the other hand, additional errors are introduced.

In the present paper, a direct discretization of the 4D equation for the DSD is retained, since the accuracy of the results is here more important than the numerical efficiency of the simulations.

* Corresponding author.
E-mail addresses: bordas@ovgu.de (R. Bordás), volker.john@wias-berlin.de (V. John), ellen.schmeyer@wias-berlin.de (E. Schmeyer), thevenin@ovgu.de (D. Thévenin).

[1] The work of R. Bordás was supported by Grant Th881/13-2 within the DFG priority programme 1276 MetStröm: Multiple Scales in Fluid Mechanics and Meteorology.
[2] The work of E. Schmeyer was supported by Grant Jo329/8-2 within the DFG priority programme 1276 MetStröm: Multiple Scales in Fluid Mechanics and Meteorology.

0045-7930/$ - see front matter © 2012 Elsevier Ltd. All rights reserved.
http://dx.doi.org/10.1016/j.compfluid.2012.05.003

Simulations based on the 4D equation can be found rather rarely in the literature. However, with increasing hardware capabilities and with modern numerical methods, this is an attractive approach since it does not require any additional assumptions, e.g., for closing the system, and it does not introduce an additional modeling error. In the used method, the turbulent flow field is simulated fully implicitly. A variational multiscale (VMS) method is applied for turbulence modeling. Several stabilized finite difference methods combined with explicit time stepping schemes are used as temporal discretization for the population balance equation. A pre-processing approach was applied to compute the collision integrals. With this numerical approach, it will be shown that the experimentally observed evolution of the DSD between the inlet of the flow domain and its outlet can be reproduced accurately. The sensitivity of the prediction with respect to varying numerical methods is studied. To our best knowledge, the combination of the used methods for simulating a population balance system cannot be found so far in the literature.

The considered configuration corresponds to an experiment proposed as a benchmark problem for the simulation of population balance systems, since:

- all data are freely available in the online database at http://www.ovgu.de/isut/lss/metstroem,
- the considered geometry and setup is simple,
- first numerical studies are already available, supporting the accuracy of the experimental measurements.

The paper is organized as follows. The experimental setup is first described in Section 2, followed by the measurements and the post-processing procedure in Section 3. Section 4 describes the population balance system used to model the experiments. The numerical methods employed to simulate this setup are discussed in Section 5 and the simulation results are presented in Section 6. A summary is given at the end of the paper.

2. Experimental setup

A special wind tunnel available at the laboratory of Fluid Dynamics & Technical Flows has been used for the present experimental investigation of disperse two-phase flows corresponding to meteorological conditions found in cumulus clouds [4,5]. This wind tunnel can be used to investigate a variety of two-phase (air/liquid) flows [12], see Fig. 1. It is a fully computer-controlled, Göttingen-type wind tunnel. Operation with a closed test section enables the controlled and reproducible investigation of two-phase mixtures in the test section. The test section is of size $H \times W \times L = 500 \times 600 \times 1500$ mm. It includes a measurement section of cross-section 450×500 mm whose windows are optically transparent in the visible spectrum. In this manner non-intrusive measurements are possible, which is essential for high-quality experimental investigations of such flows.

The disperse phase was added to the air flow with the help of an injection system. The sprays were actuated by means of eccentric screw pumps. The number of revolutions per minute (rpm) was set with the help of a frequency regulator to a prescribed value by means of a Proportional Integral Derivative (PID) regulation coded in LabView®. In order to investigate rain formation and cloud droplet interactions a full cone pneumatic atomizing nozzle was used (Type 166.208.16.12 from the company Lechler GmbH), relying on the liquid pressure principle and applying an air gauge pressure of 1.2 bar [3].

Since the influence of the support of the injection system could be noticed especially in the upper half of the measurement section, the measurement area was finally restricted to the lower half of the cross-section, see Fig. 2. The resulting velocity inhomogeneity of the air flow was then below 5% with a turbulence intensity below 7% (mean value of 2.4%). The selected nozzle shows a typical six-hole spray pattern caused by the six orifices in the nozzle. In order to reduce the influence of this pattern, the water was injected in counter-flow direction. In this way, the droplets were more homogeneously distributed, and the relative velocity difference between continuous and dispersed flow at the entrance of the measurement section was decreased, suppressing to a large extent the six-hole pattern.

3. Measurement procedure

The longitudinal coordinate of the beginning of the measurement section is defined as $x = 0$ mm. Different measurement planes perpendicular to the main flow direction were investigated, at $x = 0$ mm, $x = 200$ mm, and $x = 400$ mm, see Fig. 1. The first plane at $x = 0$ mm was measured particularly thoroughly, since it provides the information needed for the boundary condition of the numerical simulations.

Experimental measurements were systematically carried out by means of non-intrusive measurement techniques. Therefore, a small quantity of suitable tracer particles must be added to the flow. Such particles follow the structures of the continuous phase much better [1,2] than the considered droplets, allowing an indirect measure of the gas flow properties. For this reason, the velocities of both phases were measured in two separate steps.

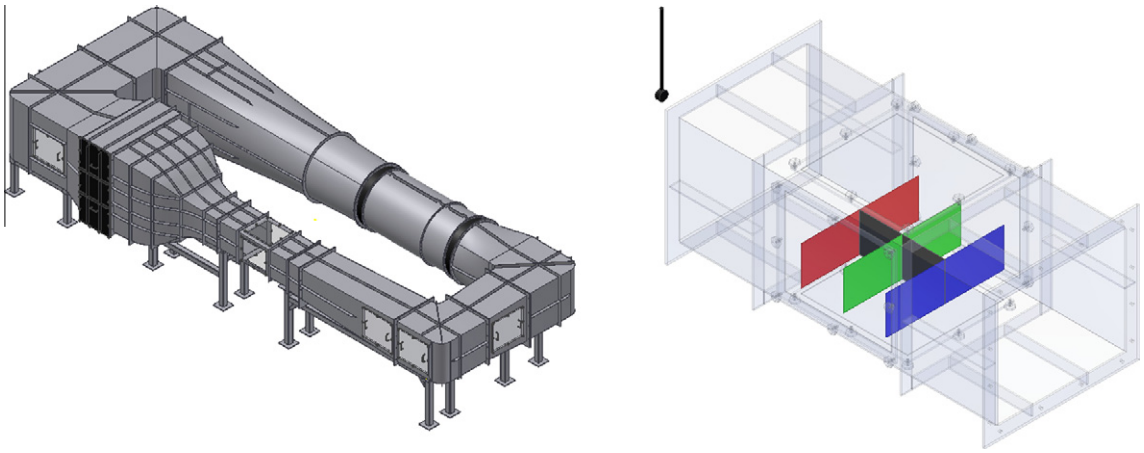

Fig. 1. Left: Göttingen-type two-phase wind tunnel with closed test section. Right: test section, with measurement planes colored.

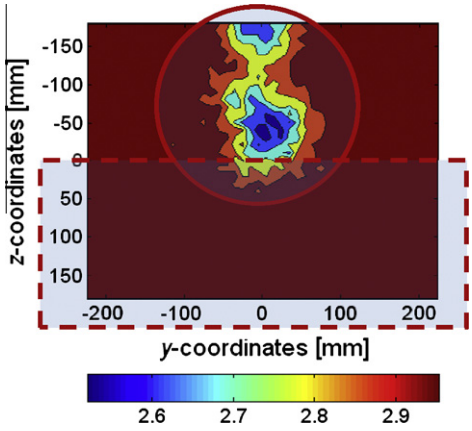

Fig. 2. Mean axial velocity distribution of the air flow at the inlet ($x = 0$ mm) of the measurement section, 630 mm downstream of the spray injection nozzle. The circle denotes the region with a noticeable influence of the injection mount and the dashed square the finally selected measurement region.

The velocity distribution of the air phase at the entrance plane ($x = 0$ mm) was measured by means of Laser-Doppler Velocimetry (LDV). During these measurements in the continuous phase, the nozzle was operating at the same pressure as in normal (spray) operation, but only with air and without water. Since the mass flow rate of air and water entering the nozzle are similar for normal operation conditions, $\dot{m}_a/\dot{m}_w = 0.4$, only minor flow changes should be induced by this necessary operation.

In order to define the locations of the measurement points for the Laser-Doppler Velocimetry and the Phase-Doppler Anemometry (PDA) techniques, a measurement grid was generated with 874 (19 in z-direction $\times$ 46 in y-direction) measurement points, with 10 mm distance in each direction between them. LDV and PDA measurements lead to a high temporal resolution. Thus, the velocity components measured in the mean flow direction (Fig. 3) included the temporal fluctuations as well. In this way, the determination of turbulence intensity was also possible.

The measured mean velocity of the air flow was $U = 2.45$ m/s. Based on U and on the hydraulic diameter of the wind tunnel ($D_H = 0.5454$ m), the Reynolds number of the flow is

$$\mathrm{Re} = \frac{U \cdot D_H}{\nu} = 8.7 \times 10^4.$$

The measured fluctuation of the air flow velocity in main flow direction was in the average $u' = 0.25$ m/s. This leads to a mean turbulence intensity of 10.9%.

The energy cascade of a turbulent flow can be estimated by post-processing PIV measurement results, as discussed for instance in [4]. Using this technique, the longitudinal integral length scale $L_{11} = 6.56$ cm was derived for the present case.

The properties of the disperse phase (water spray) were then measured separately in the three vertical planes at $x = 0$ mm, $x = 200$ mm, and $x = 400$ mm, of course using the same measurement grid as previously. For a characterization of the considered two-phase flow, the arithmetic mean diameter (D_{10}) of the water droplets is particularly important.

Velocities measured by PDA are based on the same principles as LDV. However, using PDA the simultaneous measurement of the diameter and the velocity values is possible. This allowed the investigation of the velocity-diameter correlation, as exemplified in Fig. 4. The different flow response of the droplets can be noticed in this scatter plot. Due to noticeably smaller Stokes numbers, the small droplets follow much more closely the fluctuations of the turbulent flow and are therefore associated with larger velocity fluctuations, while larger droplets tend to gather around the mean velocity value [4]. Calculating the droplet Stokes number St from the droplet properties, the integral length scale and the RMS velocity fluctuations, a maximum value of St = 0.07 is found. As a consequence, the influence of random uncorrelated particle motion (RUM) can be neglected in this configuration [38].

Having the velocity values of both phases, the relative velocity difference of the droplets can finally be calculated. This was found to be 0.3 m/s in average at $x = 0$ mm. This value reduced as expected to 0.15 m/s as the droplets reached the final measurement plane $x = 400$ mm, showing that the droplets are slightly accelerating on the way from the inlet to the outlet plane. The mean velocity of the droplets, measured by means of PDA for the planes $x = 0$ mm, $x = 200$ mm and $x = 400$ mm, is shown in Fig. 5. The data at $x = 0$ mm were used, in combination with the turbulent air flow, to extrapolate the velocity of the droplets $\mathbf{u}_{\mathrm{drop}}$ from the inlet plane to the whole domain, see Section 4.

Boundary conditions for the droplet size distribution at $x = 0$ mm have to be derived from the measurements in order to start the companion simulations. At the outlet boundary ($x = 400$ mm), experimental data are needed as well for comparison purposes. Therefore, a corresponding post-processing of the PDA measurements is necessary to obtain values for the number density or droplet concentration n [40,44]. In the present work, the approach described in [14] was finally applied, improved by a factor η_{vi} allowing to correct errors due to multiple particles occurring in the detection volume or to non-validation of particles, as described in [41]. The droplet size dependent calculation of the detection volume [41] was applied as well. Thus, the number density is finally obtained by

$$n = \frac{1}{T_{\mathrm{acq}}} \sum_{i=1}^{N_{\mathrm{sv}}} \frac{\eta_{\mathrm{vi}} \cdot t_{\mathrm{res},i}}{V_{\mathrm{det}}}, \tag{1}$$

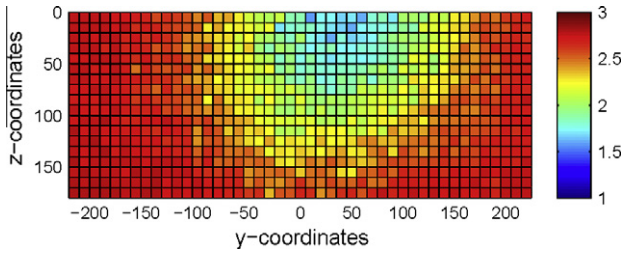

Fig. 3. Mean longitudinal velocity distribution of the air phase at $x = 0$ mm, measured by means of LDV.

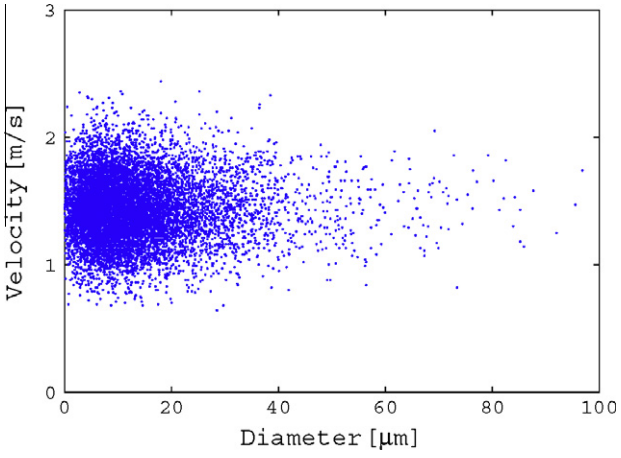

Fig. 4. Velocity-diameter correlation of the water droplets at the point $x = 0$, $y = 5$, $z = 0$.

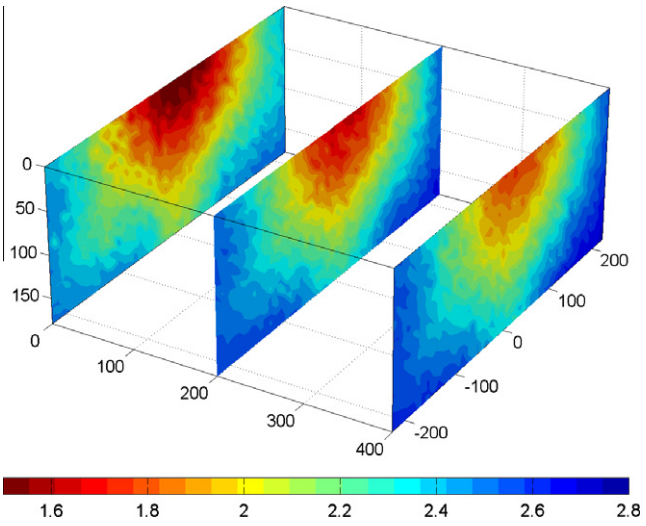

Fig. 5. Mean droplet velocity distribution in the planes $x = 0$ mm, $x = 200$ mm, and $x = 400$ mm measured by means of PDA.

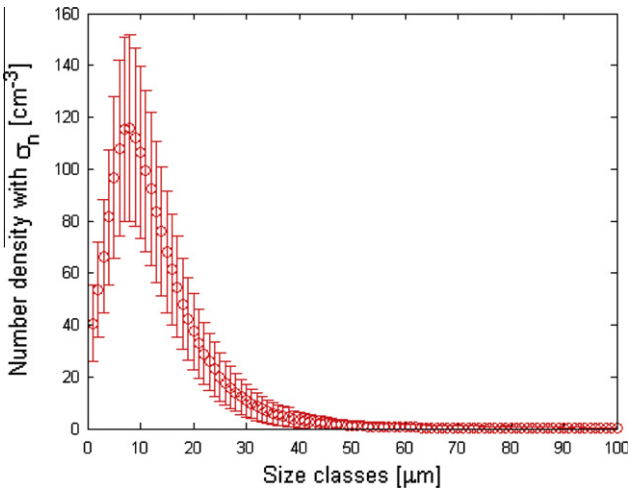

Fig. 7. Probability density function of the calculated droplet number density as a function of the size class, including the measured standard deviation as an error bar.

where T_{acq} is the acquisition time at a given measurement position, N_{sv} is the number of validated PDA-signals, η_{vi} is the correction factor described before, $t_{res,i}$ is the residence time of the ith droplet and V_{det} is the size of the PDA detection volume. The PDA detection volume is droplet size dependent and thus is a function of the droplet velocity and of the burst duration in the detection volume.

The average mean droplet number density per unit volume was finally measured to be 2000 no./cm^3 at $x = 0$ mm. The corresponding distribution of the mean values is presented in Fig. 6. Theoretically, with a droplet injection rate of 0.1 l/min and a mean droplet diameter of 12.5 µm, the corresponding droplet number density per unit volume should be indeed approximately 2000 no./cm^3, supporting the experimental measurements. This droplet number density per unit volume is in the range of typical values found in cumulus clouds [31].

The determination of the probability density function $n_k(d_k)$ is the key link between experimental data and numerical simulations. The corresponding post-processing was performed with a MATLAB® script, using the previously exported measurement raw data, and allowing both the computation of the probability density function of the droplet number density ($n_k(d_k)$) and its standard deviation ($\sigma_{n,k}$). The droplets are divided into classes (d_k) with a diameter resolution of 2 µm. The number density is computed separately for each size class using Eq. (1). In addition, the number density was calculated for different time scales by dividing the whole acquisition time T_{acq} into time intervals Δt. In this manner, the standard deviation $\sigma_{n,k}$ can be calculated with

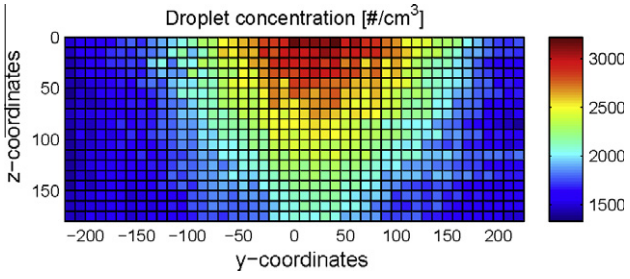

Fig. 6. Droplet number density per unit volume in no./cm^3 at $x = 0$ mm, post-processed from the PDA results.

$$\sigma_{n,k} = \sqrt{\left(\frac{1}{T_{acq}}\sum_{j=1}^{T_{acq}/\Delta t} n_{k,j}^2 \cdot \Delta t\right) - n_k^2}.$$

The input data for the simulations are then the droplet concentration as a function of the droplet diameter, together with the corresponding standard deviation, as shown in Fig. 7 for the entrance plane ($x = 0$ mm).

4. Numerical model of the process

The experiment was modeled using a coupled system consisting of the Navier–Stokes equations for describing the air flow and a population balance equation modeling the behavior of the droplet size distribution. Only the lower half of the test section was simulated, in agreement with the experimental approach described previously, see again Fig. 2.

Boundary conditions for the flow field have to be prescribed at the whole boundary of the domain used in the simulations. It is not clear if the used outflow boundary condition, associated with zero normal stresses, introduces a noticeable modeling error. For this reason, the domain for the simulations was chosen to be somewhat longer than the real measurement domain, so that the outflow boundary condition did not influence the computational results at the locations where comparisons are possible. The computational domain was set to be $\Omega = (0{,}500) \times (-225{,}225) \times (-180{,}0)$ mm^3 for x, y and z, respectively, with z corresponding to standard elevation.

The incompressible Navier–Stokes equations have the form

$$\begin{aligned} &\rho \mathbf{u}_t - 2\mu \nabla \cdot \mathbb{D}(\mathbf{u}) + \rho(\mathbf{u} \cdot \nabla)\mathbf{u} + \nabla p = \mathbf{0} \text{ in} (0, t_e) \times \Omega, \\ &\nabla \cdot \mathbf{u} = 0 \text{ in} (0, t_e) \times \Omega, \end{aligned} \tag{2}$$

where $\mathbf{u}$ (m/s) is the fluid velocity vector, p (Pa) is the pressure, $\rho = 1.2041$ kg/m^3, assumed to be constant due to the extremely low Mach number considered here, is the density of air at 293.15 K, $\mu = 18.15 \times 10^{-6}$ kg/(m s) is the dynamic viscosity of air at the same temperature, $\mathbb{D}(\mathbf{u}) = (\nabla \mathbf{u} + (\nabla \mathbf{u})^T)/2$ is the velocity deformation tensor, and t_e denotes the final time. The gravitational acceleration term was included into the pressure.

The Navier–Stokes equations, Eq. (2) have to be equipped with boundary conditions and an initial condition. The inlet condition at $\Gamma_{in} = \{0\} \times (-225, 225) \times (-180, 0)$ was directly prescribed using the time-averaged experimental velocity $\mathbf{u}_{exp}(0, y, z)$ and standard deviation $\sigma_{exp}(0, y, z)$:

$$\mathbf{u}(t,0,y,z) = \mathbf{u}_{\exp}(0,y,z) + \mathrm{rand}(t,0,y,z)\sigma_{\exp}(0,y,z)\mathbf{e}_1 \quad \text{on } (0,t_e)\times\Gamma_{\text{in}}, \tag{3}$$

where $\mathbf{e}_1$ is the Cartesian unit vector in x direction and rand $(t, 0, y, z)$ is a normally distributed random number. The computation of the random number was finally performed with the method proposed in [32], where the random number in a node is correlated to the random numbers of a prescribed number of neighbor nodes and to the local random numbers used at some previous discrete times. The second and third component of the inlet velocity were set to be zero. At the outlet $\Gamma_{\text{out}} = \{500\}\times(-225, 225)\times(-180, 0)$, outflow boundary conditions

$$(2\nu\mathbb{D}(\mathbf{u}) - p\mathbb{I})\cdot\mathbf{n} = \mathbf{0} \quad \text{on } (0,t_e)\times\Gamma_{\text{out}},$$

were used. Here, $\mathbf{n}$ denotes the outward pointing normal vector on the boundary. Along the top boundary $\Gamma_{\text{top}} = \{0{,}500\}\times(-225, 225)\times\{0\}[\text{m}^3]$, a free slip boundary condition without penetration was implemented

$$\mathbf{u}\cdot\mathbf{n} = 0 \quad \text{on } (0,t_e)\times\Gamma_{\text{top}},$$
$$\mathbf{n}^T(2\nu\mathbb{D}(\mathbf{u}) - p\mathbb{I})\boldsymbol{\tau}_k = 0 \quad \text{on } (0,t_e)\times\Gamma_{\text{top}},\ k = 1,2,$$

where $(\mathbf{n}, \boldsymbol{\tau}_1, \boldsymbol{\tau}_2)$ is an orthonormal system of vectors. This boundary condition models a symmetry plane. On all other boundaries $\Gamma = \partial\Omega\backslash(\Gamma_{\text{in}}\cup\Gamma_{\text{out}}\cup\Gamma_{\text{top}})$, free slip with penetration conditions were used

$$\mathbf{n}^T(2\nu\mathbb{D}(\mathbf{u}) - p\mathbb{I})\mathbf{n} = 0 \quad \text{on } (0,t_e)\times\Gamma,$$
$$\mathbf{n}^T(2\nu\mathbb{D}(\mathbf{u}) - p\mathbb{I})\boldsymbol{\tau}_k = 0 \quad \text{on } (0,t_e)\times\Gamma,\ k = 1,2.$$

These boundary conditions model the case that there are fluctuations on Γ which are directed inside and outside the domain. This corresponds to the experimental setup since the boundaries of the measured volume are slightly away from the walls of the wind tunnel. To obtain an initial condition, the flow was simulated until it was fully developed. An instantaneous flow field was then saved and used as initial flow field in all simulations.

The DSD was modeled by a population balance equation. This model includes transport, growth, and coalescence of droplets. It has the form

$$\frac{\partial f}{\partial t} + \frac{\partial}{\partial d}\left(\frac{a}{d}f\right) + \nabla\cdot(f\mathbf{u}_{\text{drop}}) = \frac{d^2}{2}\int_{d_{\min}}^{d}\frac{\kappa_{\text{col}}((d^3-(d')^3)^{1/3},d')}{(d^3-d'^3)^{2/3}}f(\cdot,(d^3-(d')^3)^{1/3})f(\cdot,d')\,dd' - f(\cdot,d)\int_{d_{\min}}^{d_{\max}}\kappa_{\text{col}}(d,d')f(\cdot,d')\,dd' \quad \text{in } (0,t_e)\times\Omega\times(d_{\min},d_{\max}), \tag{4}$$

where $f\,(\text{m}^4)$ is the droplet size distribution, $d\,(\text{m})$ is the diameter of the droplets with $d\in[d_{\min}, d_{\max}]$, $\mathbf{u}_{\text{drop}}$ (m/s) is the velocity of the droplets, $a\ (\text{m}^2/\text{s})$ is the growth rate, and $\kappa_{\text{col}}\ (\text{m}^3/\text{s})$ is the collision kernel. The transport due to random uncorrelated motion (RUM) is not taken into account in Eq. (4), since it is negligible in the present case, as discussed previously.

The experimental data for the air velocity and for the droplet velocity at the plane $x = 0$ m were extrapolated constantly into Ω, e.g., $\mathbf{u}_{\text{drop,exp}}(x,y,z) = \mathbf{u}_{\text{drop,exp}}(0,y,z)$ for all $x\in[0, 0.5]$ m. These values were subtracted from the experimental data of the time-averaged velocity of air, giving a time-averaged velocity difference between continuous (air) and the disperse (water droplets) phases. This difference was subtracted from the first component of the velocity of air computed by the Navier–Stokes equations, Eqs. (2) to define the first (longitudinal) component of the droplet velocity $\mathbf{u}_{\text{drop}}$

$$(\mathbf{u}_{\text{drop}})_1 := \text{extrapol}(\mathbf{u}_{\text{drop,exp}}) + (\mathbf{u}_{\text{air,sim}})_1 - \text{extrapol}(\mathbf{u}_{\text{air,exp}}).$$

The other components of the droplet velocity were just prescribed as the velocity components coming from the solution of Eq. (2). With the described approach, the turbulent character of the flow field computed with Eq. (2) can be carried over to $\mathbf{u}_{\text{drop}}$.

A model for the growth rate was derived in [39] by considering individual droplets

$$a = \frac{4(S-1)}{\left[\left(\frac{L}{R_vT}-1\right)\frac{L\rho_L}{KT} + \frac{\rho_L R_v T}{De_s(T)}\right]},$$

where S is the saturation, $L = 2.453\times10^6$ J/kg the latent heat, $R_v = 461.5$ J/(kg K) is the gas constant for water vapor, $T = 293.15$ K is the temperature, $\rho_L = 998.21$ kg/m^3 is the density of water, $K = 2.55\times10^{-2}$J/(ms K) is the thermal conductivity of air at the considered temperature [39], $D = 2.52\times10^{-5}$ m^2/s is the diffusion coefficient of water vapor in air at $T = 293.15$ K and 100 kPa [39], and $e_s(T) = 2338.54$ Pa is the equilibrium vapor pressure at 293.15 K. The factor 4 occurs in the previous equation because the diameter of the droplets was considered instead of the radius, as in [39]. In all present simulations, a super saturation of 1% ($S = 1.01$) was assumed, which is a typical value for clouds (see Chapter 13 in [36]) and corresponds to an estimation of the maximum value found in the wind tunnel experiments, leading to

$$a = 5.0613\cdot10^{-12}\ \text{m}^2/\text{s}.$$

The model employed for the coalescence follows [17,35]. The first term models the production of droplets of diameter d due to the coalescence of smaller droplets. The second term in the model accounts for the disappearance of droplets of diameter d because of their coalescence with other droplets. For the collision kernel κ (m^3/s), the two main physical processes (Brownian motion and shear) were combined, leading to the sum of two contributions

$$\kappa_{\text{col}}(d,d') = C_{\text{brown}}\frac{2k_BT}{3\mu}(d+d')\left(\frac{1}{d}+\frac{1}{d'}\right) + C_{\text{shear}}\times\sqrt{2\nabla\mathbf{u}_{\text{drop}}:\nabla\mathbf{u}_{\text{drop}}}(d+d')^3. \tag{5}$$

Here, $k_B = 1.3806510^{-23}$ J/K is the Boltzmann constant. The two dimensionless model parameters, C_{brown} and C_{shear}, will be later calibrated by fitting the numerical results to experimental data.

The experimental data obtained for the droplet number density n (in no./cm^3), see Eq. (1), had to be converted first to a droplet size distribution f (in no./m^4). This was achieved in the following way. For each class, the number of drops n_i (in no./cm^3) was experimentally given as well as its standard deviation $\sigma_{n,i}$ (in no./cm^3). Following for instance [39] (Eq. 2.3.2), the total number of drops per unit volume of physical space is given by

$$n_{\text{tot}}(t,\mathbf{x}) = \int_{d_{\min}}^{d_{\max}} f(t,\mathbf{x},d)\,dd.$$

For the time–averaged values at the inlet, it is

$$n_{\text{tot,in}}(\mathbf{x}) = \int_{d_{\min}}^{d_{\max}} f_{\text{in,exp}}(\mathbf{x},d)\,dd = \sum_{i=0}^{n_d} n_i. \tag{6}$$

Assuming $f_{\text{in,exp}}(\mathbf{x}, d)$ to be for each $(\mathbf{x}, d)$ a continuous function, the composite midpoint rule of numerical quadrature gives

$$\int_{d_{\min}}^{d_{\max}} f_{\text{in,exp}}(\mathbf{x},d)\,dd = \sum_{i=0}^{n_d}\int_{d_i}^{d_{i+1}} f_{\text{in,exp}}(\mathbf{x},d)\,dd \approx \sum_{i=0}^{n_d}(d_{i+1}-d_i)f_{\text{in,exp}}(\mathbf{x},d_{i+1/2}). \tag{7}$$

From Eqs. (6) and (7) it follows that

$$f_{\text{in,exp}}(\mathbf{x}, d_{i+1/2}) \approx \frac{n_i}{d_{i+1} - d_i} \left[\frac{\text{no.}}{\mu\text{m cm}^3}\right] = 10^{12} \frac{n_i}{d_{i+1} - d_i} \left[\frac{\text{no.}}{\text{m}^4}\right]. \quad (8)$$

For the conversion of the experimental number density to the droplet size distribution, equality in the first step of relation Eq. (8) was assumed and the droplet size distribution was linearly interpolated. The standard deviation was scaled the same way, i.e.,

$$\sigma_{f,i}(\mathbf{x}, d_{i+1/2}) = 10^{12} \frac{\sigma_{n,i}}{d_{i+1} - d_i} \left[\frac{\text{no.}}{\text{m}^4}\right].$$

The initial condition was given by

$$f(0, \mathbf{x}, d) = 0 \quad \text{in } \Omega \times (d_{\min}, d_{\max}),$$

i.e. there were no droplets in the flow domain.

Due to the boundary conditions for the flow field at the boundary Γ, which allow fluctuations on Γ to be directed outside the domain, droplets might leave the computational domain. The transport of droplets through the lateral walls because of fluctuations which are directed into the domain was not taken into account since no experimental data were available for this process. In all numerical studies, it turned out that the loss of droplets due to the outflow through the lateral boundaries was negligible. In addition, because of the positive growth rate, a boundary condition for the smallest droplet size $d_{\min}$ is necessary, as a simple model for the nucleation of droplets. For this issue, experimental data were not available. To circumvent this difficulty, an artificial smallest diameter of the droplets was introduced, $d_{\min,\ \text{art}} = 0$ m, and the boundary condition for the inlet was finally set to be

$$f(t, \mathbf{x}, d) = \begin{cases} f_{\text{in,exp}}(0, \mathbf{x}, d) + \text{rand}(t, \mathbf{x})\sigma_f(\mathbf{x}, d), & \mathbf{x} = (0, y, z) \in \Gamma_{\text{in}}, \\ 0, & \text{at } d = d_{\min,\text{art}}, \end{cases} \qquad t \in (0, t_e),$$

where white noise was used for computing rand $(t, \mathbf{x})$. Here, the computation of the random number was performed with the Box–Muller scheme. The boundary condition of the DSD at the inlet was thus defined as a normally distributed perturbation of the time-averaged experimental data which was linearly interpolated. In $[d_{\min,\text{art}}, d_{\min})$, the DSD was set to be $f(d) = 0$. Values of the DSD for such small parameters are needed in the production term of the collision integral since $(d^3 - (d')^3)^{1/3}$ tends to zero for $d' \to d$. This definition prevents the kernel and the terms in the integrals from being singular.

5. Numerical methods

The numerical studies presented below were based on non-dimensional equations using the following reference values

$$l_\infty = 1 \text{ m}, \quad u_\infty = 1 \text{ m/s}, \quad t_\infty = \frac{l_\infty}{u_\infty} \text{ s}, \quad p_\infty = \rho u_\infty^2 \text{ Pa},$$
$$f_\infty = 10^{12} \text{ 1/m}^4, \quad d_\infty = d_{\max} = 1.71 \times 10^{-4} \text{ m}.$$

The minimal diameter of the droplets was taken from the experimental data to be $d_{\min} = 10^{-6}$ m.

The domain Ω was triangulated with a $50 \times 45 \times 18$ hexahedral grid, equi-distant in each direction. With this grid, the positions of the measurement points were located at nodes. In addition, the mesh for the internal coordinate was chosen in such a way that a direct fitting of the experimental data was possible. Since the data were given for equi-distributed diameters, the grid for the internal coordinate was defined in the same way. Only the interval $(0, d_{\min})$ had a different length.

An implicit time stepping scheme and an inf-sup stable finite element method formed the basis of the discretization of the Navier–Stokes Eq. (2). As time stepping scheme, the Crank–Nicolson method was applied. This scheme is widely used since it leads to a good compromise between accuracy and efficiency [26]. The length of the equi-distant time step was set to be $\Delta t = 0.001$ s or alternatively $\Delta t = 0.0005$ s with a final time $t_e = 1$ s.

After having applied the Crank–Nicolson scheme and a fixed point iteration as linearization, the equations were discretized in each discrete time with the Q_2/P_1^{disc} finite element method. Hence, the velocity was approximated with continuous piecewise second-order polynomials and the pressure with discontinuous piecewise linear functions. This pair of finite element spaces has been identified as one of the best performing finite element approaches for the simulation of incompressible Navier–Stokes equations in numerous studies [11,18,20]. On the used grid, this finite element discretization leads to 1020201 degrees of freedom for the velocity and to 162000 degrees of freedom for the pressure. The implementation of the slip and penetration boundary conditions in the framework of finite element methods is described in [19].

Since the flow is turbulent, numerical simulations require the application of a turbulence model. In the simulation presented in Section 6, a finite element variational multiscale (VMS) method was applied [6,7]. In VMS methods, the scale separation is obtained by projections into appropriate function spaces. In this way, resolved large scales $P\bar{\mathbf{u}}$, resolved small scales $(I - P)\bar{\mathbf{u}}$, and unresolved scales $\mathbf{u}'$ are defined, where $\mathbf{u} = P\bar{\mathbf{u}} + (I - P)\bar{\mathbf{u}} + \mathbf{u}'$, P is an L^2–projector, and I is the identity operator. The resolved scales $\bar{\mathbf{u}}$ will be simulated. The idea of scale separation in resolved and unresolved scales is like in traditional large eddy simulation (LES). However, the application of a projection for defining the scale separation is a fundamental difference to LES, as in LES the large scales are defined by spatial averaging. There are meanwhile a number of realizations of VMS methods, see [9,28] for overviews. A number of studies show that the VMS approach is competitive with LES methods and that it leads often even to better results [10,16,37].

In the simulations presented below, the method from [22] was applied, together with the extension of choosing the projection space adaptively which was introduced in [24]. The VMS methods from [22,24] require the definition of a tensor-valued projection space and the use of an eddy viscosity model. In the method from [22], the local projection space is the same in the whole domain. Usually, piecewise constant tensors (VMS-P0) or discontinuous piecewise linear tensors are applied. Experience shows that the constant tensors should be preferred [23,28]. An a posteriori and locally adaptive choice of the projection space was proposed in [24]. This choice is based on an indicator for the local turbulence intensity. In the simulations presented in Section 6, the same parameters in the adaption process were used as suggested in [24].

A main feature of the projection–based VMS methods is that the eddy viscosity model acts directly only on the resolved small scales. This is another fundamental difference to LES methods, where the eddy viscosity model acts on all resolved scales. In a number of studies, it was observed that rather simple eddy viscosity models applied within the framework of VMS methods often lead to good results [10,15]. In the simulations presented below, the static Smagorinsky model $C_S\delta^2\|\mathbb{D}(\bar{\mathbf{u}})\|$ from [43], was used, with $C_S = 0.005$ and δ being the length of the shortest edge of a mesh cell.

The number of grid points for discretizing the equation for the DSD was 3 967 086. In [29,30], it was shown that different discretizations for this equation might lead to different results for quantities of interest. Considering that the residence time of the droplets in the domain is rather short (such that only small differences of the results obtained with different discretizations can be expected), that finite element methods are quite expensive in high dimensions (in particular stabilized methods and variational mul-

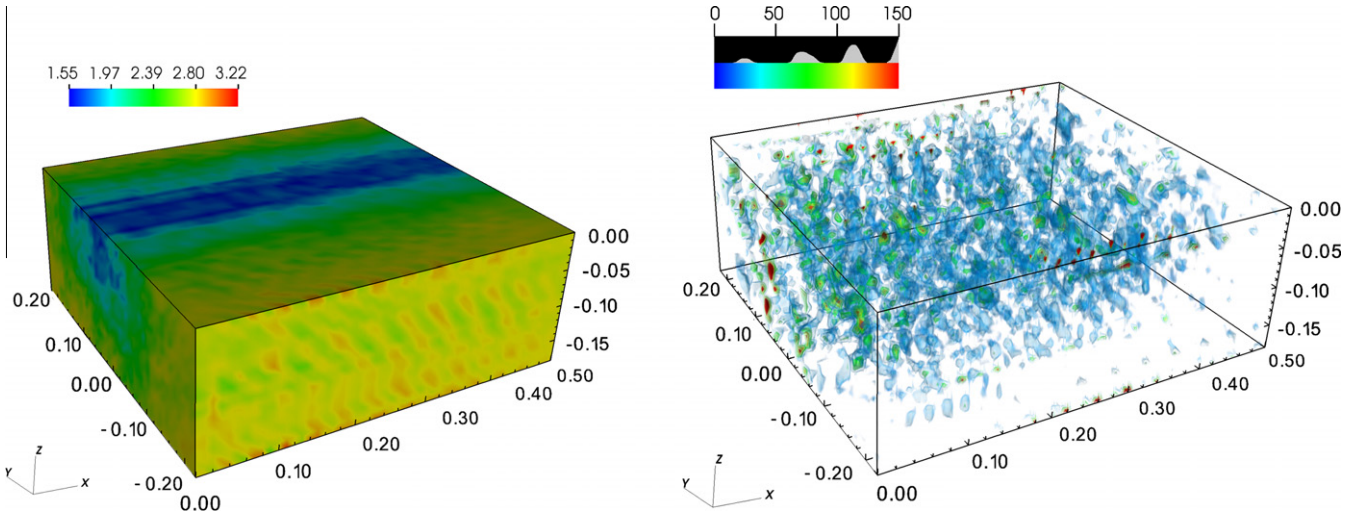

Fig. 8. Instantaneous velocity field obtained from a simulation: magnitude of the velocity vector (left) and Q-criterion (right). The inflow boundary of the measurement section ($x = 0$ mm) is on the left hand side (front part of the picture). The symmetry plane lies on top of the graphical representation.

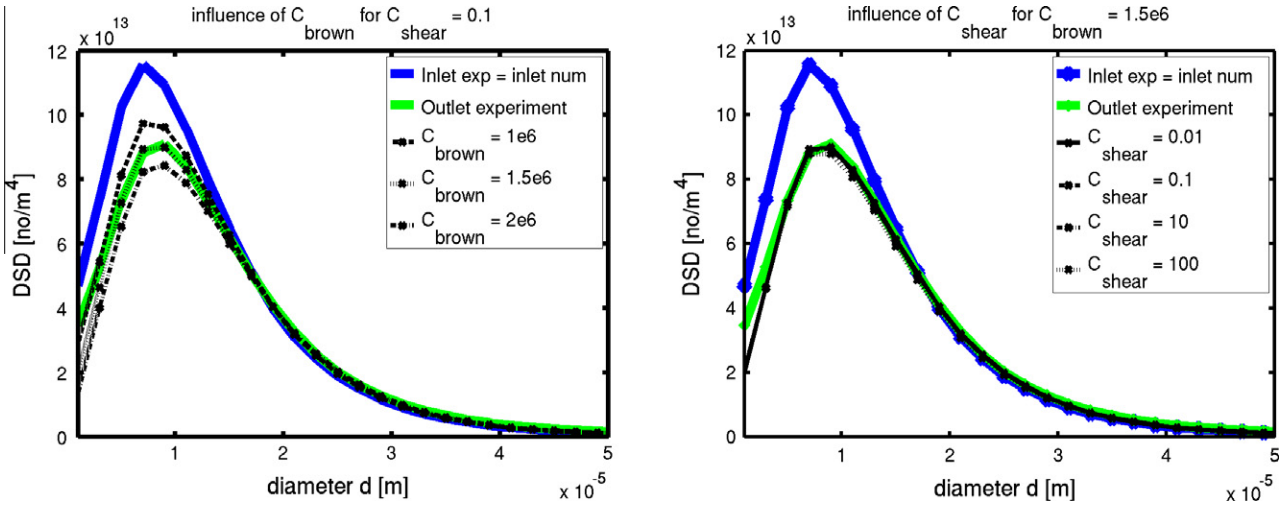

Fig. 9. Calibration of the model parameters C_{brown} and C_{shear}, with VMS-ADAP, RK-ENO, and $\Delta t = 0.001$. The green curves are the averaged experimental data at the outlet of the measurement volume.

tiscale methods), and that the DSD is defined in a 4D tensor-product domain, we applied finite difference methods for the discretization of (4): simple upwinding with forward Euler time-stepping (FWE–UPW), simple upwinding with the backward Euler scheme (BWE–UPW), and an essentially non-oscillatory (ENO) scheme of order three with an optimal, explicit, third order, total variation diminishing (TVD) Runge–Kutta method (RK-ENO). The last scheme has been shown to deliver a good ratio between accuracy and efficiency in recent studies [27]. It was preferably used in the numerical simulations presented below. For the temporal discretization of (4), the same time steps were applied as they were used in the temporal discretization of the Navier–Stokes equations.

The evaluation of the collision integrals on the right hand side of Eq. (4) was based on a pre-processing step. This step will now be described exemplarily for the second term in Eq. (4). In this discussion, the dependency of the DSD on time and space will be neglected.

Let $0 = d_0 < d_1 = d_{min} < \cdots < d_N = d_{max}$ be the grid points with respect to the internal coordinate. As explained above, $f(d)$ vanishes in (d_0, d_1). Otherwise, the DSD was assumed to be continuous.

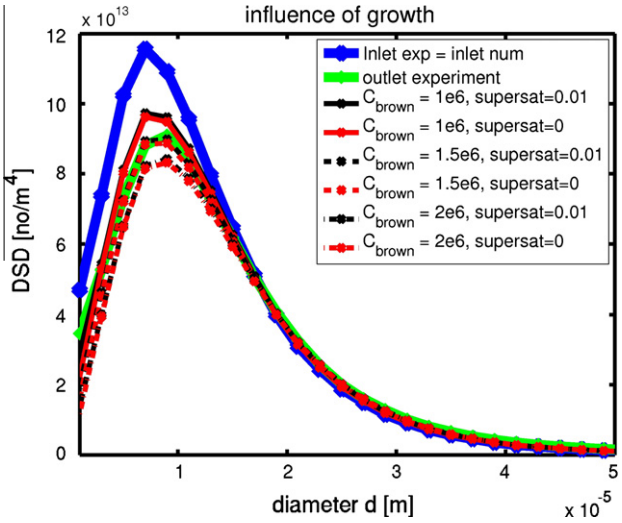

Fig. 10. Impact of the growth term in Eq. (4) on the DSD, simulations with VMS-ADAP, RK-ENO, $C_{shear} = 0.1$, and $\Delta t = 0.001.1$

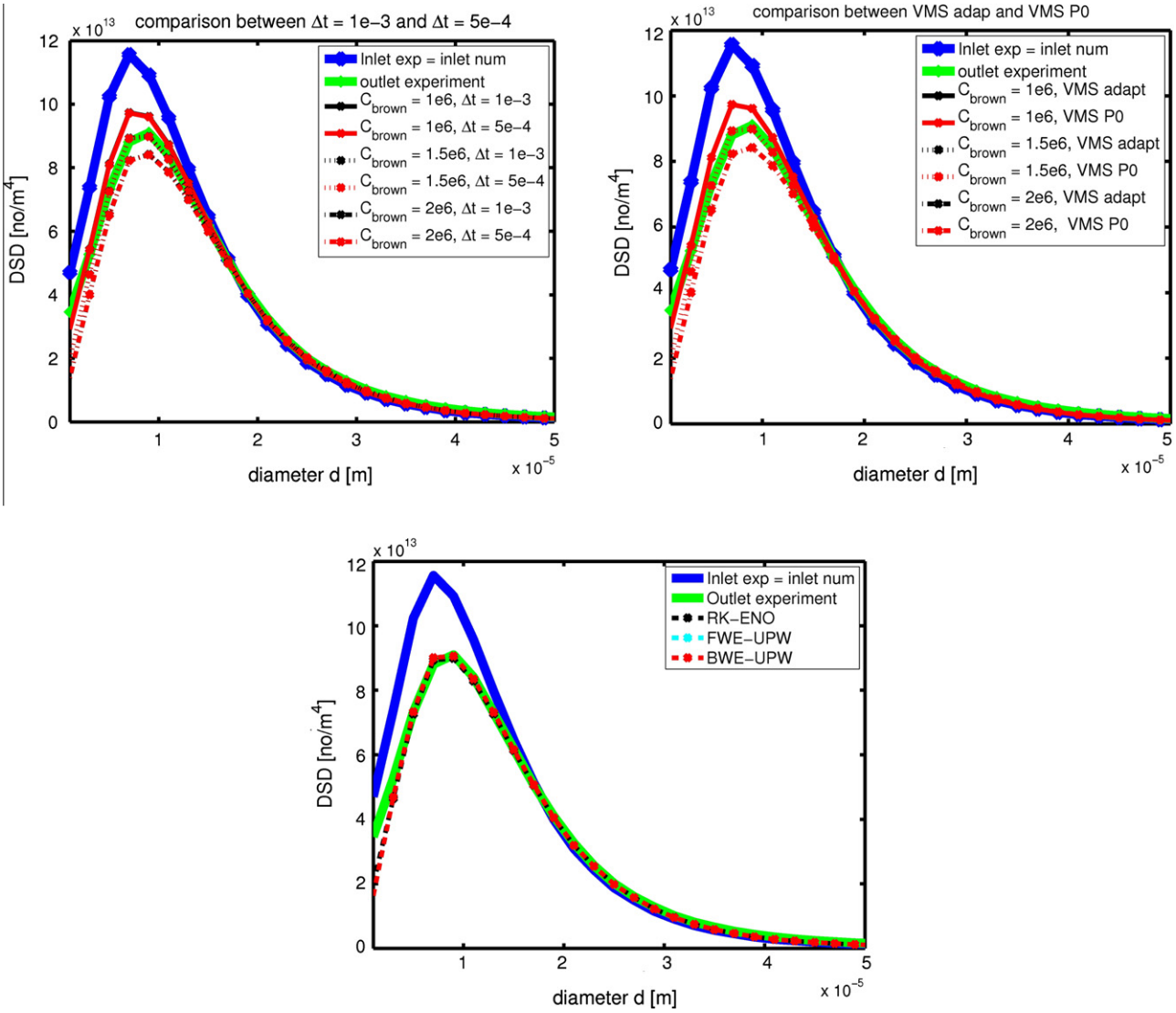

Fig. 11. Sensitivity of the space–time averaged DSD. Upper left: with respect to Δt, with VMS-ADAP, RK-ENO. Upper right: with respect to the turbulence model, with RK-ENO and $\Delta t = 0.001$. Bottom: with respect to the discretization of the equation for the DSD, with VMS-ADAP and $\Delta t = 0.001$. Note that some curves are hardly visible since they lay on top of each other.

Then, the integral for the second term in Eq. (4) at the diameter d_j, $j \in \{1, \ldots, N\}$, was approximated by

$$f(d_j)\int_{d_{\min}}^{d_{\max}} \kappa_{\mathrm{col}}(d_j, d) f(d')\, dd' = f(d_j)\sum_{i=1}^{N-1}\int_{d_i}^{d_{i+1}} \kappa_{\mathrm{col}}(d_j, d') f(d')\, dd'$$
$$\approx f(d_j)\sum_{i=1}^{N-1}\frac{f(d_{i+1}) + f(d_i)}{2} \times \int_{d_i}^{d_{i+1}} \kappa_{\mathrm{col}}(d_j, d')\, dd'.$$

The remaining integrals depend only on the kernel and the grid for the internal coordinate

$$\int_{d_i}^{d_{i+1}} \kappa_{\mathrm{col}}(d_j, d')\, dd' = C_{\mathrm{brown}}\frac{2k_B T}{3\mu}\int_{d_i}^{d_{i+1}} (d + d')\left(\frac{1}{d} + \frac{1}{d'}\right) dd'$$
$$+ C_{\mathrm{shear}}\sqrt{2\nabla \mathbf{u}_{\mathrm{drop}} : \nabla \mathbf{u}_{\mathrm{drop}}}\int_{d_i}^{d_{i+1}} (d + d')^3\, dd',$$

$i = 1, \ldots, N-1$. Since the grid is given, the integrals on the right hand side can be computed in a pre-processing step. A similar approach can be performed for the first integral in Eq. (4). For the evaluation of the integrals, the package MAPLE was used, since it was not possible to evaluate all integrals analytically. The numerical computation of the integrals in MAPLE was performed with the option to be exact for 14 digits.

Each step of the fixed point iteration for the implicitly discretized Navier–Stokes equations requires the solution of a linear saddle point problem. These problems were solved iteratively with a preconditioned flexible GMRES method [42]. As preconditioner, the multiplicative Vanka method [45], which is a block Gauss–Seidel scheme, was applied. A similar approach, where the Vanka method was embedded as smoother in a multigrid method, has been proved to be an efficient solver for inf-sup stable finite element discretizations of incompressible Navier–Stokes equations, see [21] and the references therein. Note that in the present example the construction of the grid, such that the nodes correspond to the measurement points, prevented the use of a multigrid method since coarse grids are not available.

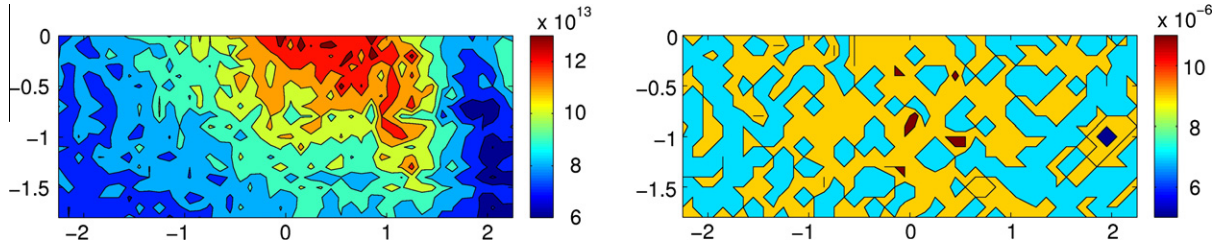

Fig. 12. Experimental results at outlet: peak value of the DSD in no./m^4 (left) and corresponding droplet diameter for which this value is attained (right). Same scales as Fig. 13.

Using the backward Euler scheme for the temporal discretization of the equation for the DSD (4) likewise requires the solution of a linear system of equations in each discrete time. These systems were also solved iteratively with the BiCGStab method [42] and the SSOR method as preconditioner. Generally, only few iterations were necessary since the solution from the previous discrete time constituted a good initial iterate for the short time steps employed during integration.

6. Numerical studies

The purposes of the numerical studies were twofold. On the one hand, several features of the employed models will be investigated, like appropriate values for the model constants of the collision kernel. Additionally, the impact of the different numerical methods from Section 5 on the computed results will be studied. Such investigations are useful to quantify the sensitivity of the results with respect to the numerical schemes.

All simulations were performed with the code MooNMD [25] on a HP BL680c computer with 2400 MHz Xeon processors. The used code is an academic research code including many finite element methods and applicable to several classes of problems. Hence it is not specifically optimized for the considered application. In addition, parallelization has not been completed yet. The simulation of one time step required between 130 and 250 s, depending on the method.

Fig. 8 presents an instantaneous view of the computed velocity field together with the Q-criterion [13] applied to the velocity field. It can be clearly seen that the flow in the center of the channel is slower due to the nozzle mount placed upstream of the measurement section. The residence time of a droplet in the measurement volume is typically below 0.5 s.

The first purpose of the numerical studies was the calibration of the unknown parameters C_{brown} and C_{shear} in the collision kernel, Eq. (5). The calibration was performed by fitting the computed DSD to the experimental data. From the experiments, the DSD was available at each measurement point of the outlet plane ($x = 400$ mm). Due to the turbulent character of the flow, the experimental data, which are already time-averaged, differ notably at measurement points. For this reason, an averaging in space was applied to the data, leading to one space–time-averaged curve to compare with. The same space–time-averaging was applied to

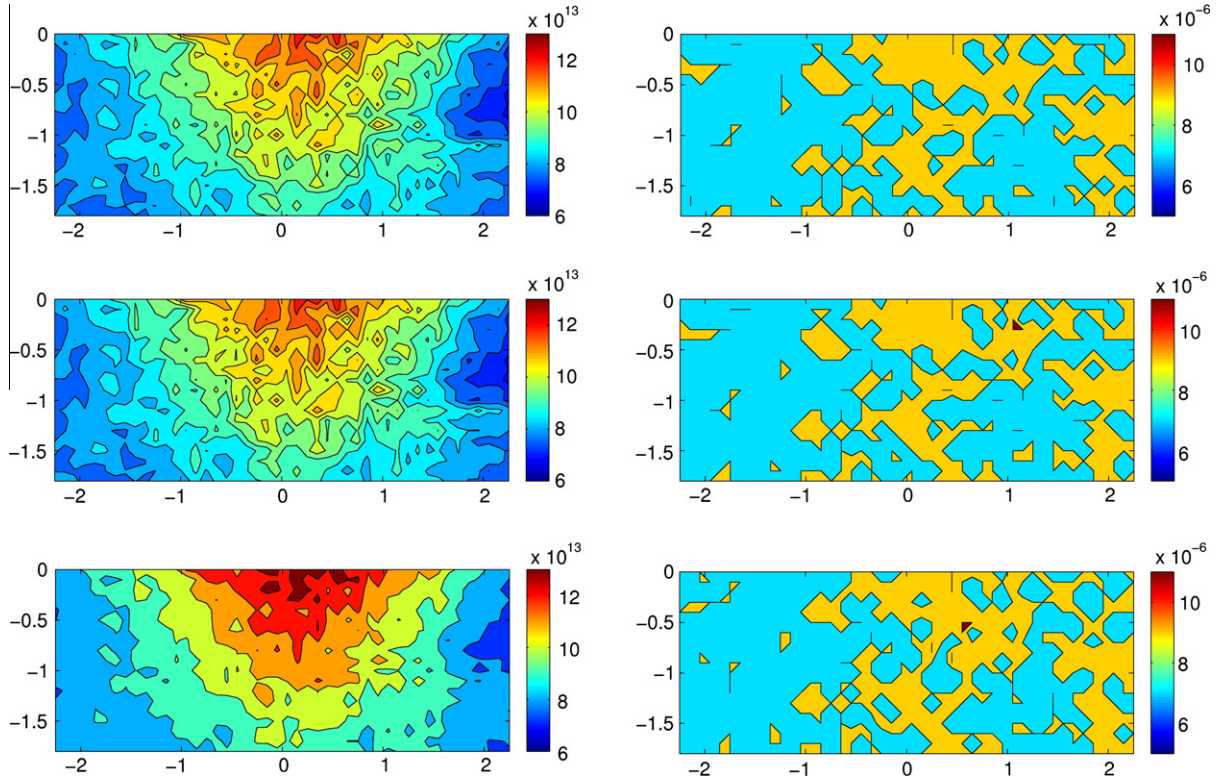

Fig. 13. Simulated results at outlet: peak value of the DSD in no./m^4 (left) and corresponding droplet diameter for which this value is attained (right). On top: using FWE-UPW; middle: using BWE-UPW; bottom: using RK-ENO. All simulations with VMS-ADAP, $C_{\text{brown}} = 1.5 \times 10^6$, $C_{\text{shear}} = 0.1$, and $\Delta t = 0.001$. Same scales as Fig. 12.

the computational results as well, with a time-averaging performed in the interval [0.5,1] s.

Fig. 9 presents results for the calibration of the parameters C_{brown} and C_{shear}. After a manual trial and error procedure, it has been found that for appropriately chosen parameters, i.e., $C_{brown} \simeq 1.5 \times 10^6$ and $C_{shear} \simeq 0.1$, the change of the droplet size distribution observed in the experiments from the inlet to the outlet is very well reproduced by the numerical simulations. Considering the order of magnitude difference between C_{brown} and C_{shear}, one should keep in mind that the term of the collision kernel referring to Brownian motion contains as well the extremely small factor k_B, see Eq.(5). For small droplets, the last factor in this term becomes large so that in this case the collision associated to Brownian motion dominates, as expected from the physics. On the other hand, for larger droplets (typically for $d \gtrsim 7\,\mu m$), shear-induced collision and hence the parameter C_{shear} becomes essential to fit the experimental data correctly. It should be noted that the used model for the DSD possesses only one direction, namely that larger droplets are created from smaller ones, by coalescence or by growth. Hence, a good prediction of the small droplets is a necessary basis for a good prediction of the large droplets.

A second aspect of the investigated model is the importance of growth and coalescence. From the setup of the experiments, it can be expected that coalescence is the dominating mechanism. This dominance was numerically verified by comparing results without the growth term in Eq. (4) and with including this term using a realistic value for the supersaturation. Fig. 10 shows that the impact of the growth term on the simulated DSDs is in fact negligible.

Last, studies will be presented on the impact of using different numerical methods on outputs of interest. The sensitivity of the computed space–time-averaged DSD with respect to the various numerical methods is illustrated in Fig. 11. It can be seen that neither the length of the time step, nor the turbulence model, nor the discretization of the equation for the DSD lead to noticeable differences in the results. Hence, the computational results for the space–time-averaged DSD at the outlet are rather insensitive with respect to the applied numerical methods.

More details of the computed DSDs can be studied by considering for instance the time-average of the DSDs at the outlet plane ($x = 400$ mm). Figs. 12 and 13 present a comparison between experimental and numerical data obtained for this quantity of interest. The main experimental features (peak of the DSD for larger droplets at the outlet, while peak values become smaller) correspond well to the space–time-averaged curves presented in Figs. 9–11.

The results obtained with different numerical methods for discretizing the DSD are compared in Fig. 13. All results are physically correct: the maximal values of the DSDs decrease and the corresponding diameters increase. However, slight differences appear depending on the method when comparing to the experimental data. One reason might be that the random perturbation at the inlet is only an approximation of the physical phenomena occurring in the experiments. Furthermore, the experimental measurements are associated as well with some level of uncertainty. As a whole, there are only little differences between the numerical results obtained with FWE–UPW and BWE–UPW. Using RK-ENO, slightly higher peak values are obtained. This result is due to the property that the ENO discretization is less diffusive than the upwind method [27].

7. Summary

The properties of a turbulent two-phase flow (air with a spray of water droplets smaller than 50 μm in diameter) has been experimentally investigated in a dedicated wind tunnel. The velocity of both phases have been measured as well as the Droplet Size Distribution for different positions within the test section. The droplet diameters measured as a function of time have been converted into a droplet number density as a function of different size classes using a post-processing method. The velocity of the air flow, including its temporal change is used as boundary condition for the continuous phase at the inlet, which is modeled by the Navier–Stokes equations. The turbulent flow field is simulated by a finite element variational multiscale (VMS) method.

The measured droplet size distribution (in the form of number density) and velocity information are used in the simulations both as inflow boundary condition for the disperse phase and for a quantitative comparison between experiments and numerical predictions at the outlet. The evolution of the droplet population is modeled by an equation for the DSD, including transport, growth, and coalescence of droplets. The equation for the DSD is defined directly in a 4D domain, including the diameter of the droplets, to be able to perform accurate simulations.

After calibrating the unknown parameters of the collision kernel by fitting the computed DSD to experimental data, the resulting comparison between experiments and simulations is very promising. With appropriately chosen parameters, only small differences could be observed for the space–time-averaged DSDs at the outlet computed with different numerical schemes.

The developed computational procedure will now be used to investigate in more detail similar issues of increasing complexity, first considering the interaction between two sprays with different initial Droplet Size Distributions, in order to quantify the observed modifications concerning droplet collisions. The influence of the saturation parameter will also be investigated, in parallel to corresponding experiments in the same setup.

References

[1] Bordás R, Bendicks C, Kuhn R, Wunderlich B, Thévenin D, Michaelis B. Coloured tracer particles employed for 3D-PTV in gas flows. In: Prenel JP, Bailly Y. editors, 13th international symposium on flow visualization. Nice, France; 2008. p. 093/1–093/12.
[2] Bordás R, Fellegi G, Wunderlich B, Kuhn R, Thévenin D, Michaelis B. Appropriate tracers to measure velocities in particle-laden gas flows using optical techniques. In: Sommerfeld M, Tropea C. editor, 6th international conference on multiphase flow, ICMF 2007. Leipzig, Germany; 2007. p. S7/1–7.
[3] Bordás R, Hagemeier T, Thévenin D. Experimental investigation of droplet-droplet interactions. In: 23rd European conference on liquid atomization and spray systems. Brno, Czech Republic; 2010. p. 198.1–198.6.
[4] Bordás R, Hagemeier T, Wunderlich B, Thévenin D. Droplet collisions and interaction with the turbulent flow within a two-phase wind tunnel. Phys Fluids 2011;23(085105):1–11.
[5] Bordás R, Thévenin D. Modeling cumulus clouds in a two-phase wind tunnel. In: European geosciences union general assembly EGU 2009. Vienna, Austria; 2009. Poster 4722.
[6] Farge M, Schneider K. Coherent Vortex Simulation (CVS), a semi-deterministic turbulence model using wavelets. Flow Turb Combust 2001;66:393–426.
[7] Farge M, Schneider K, Pellegrino G, Wray AA, Rogallo RS. Coherent vortex extraction in three-dimensional homogeneous turbulence. Phys Fluids 2003;15:2886–96.
[8] Ganesan S. An operator-splitting Galerkin/SUPG finite element method for population balance equations : stability and convergence. ESAIM M2AN 2012;46:1447–65.
[9] Gravemeier V. The variational multiscale method for laminar and turbulent flow. Arch Comput Meth Eng 2006;13:249–324.
[10] Gravemeier V. Variational multiscale large eddy simulation of turbulent flow in a diffuser. Comput Mech 2007;39:477–95.
[11] Gresho PM, Sani RL. Incompressible flow and the finite element method. Chichester: Wiley; 2000.
[12] Hagemeier T, Bordás R, Bencs P, Wunderlich B, Thévenin D. Determination of droplet size and velocity distributions in a two-phase wind tunnel. In: Bailly Y, Prenel JP. editor, ISFV13 – 13th international symposium on flow visualization, Nice, France; 2008. p. 094/1–094/10.
[13] Haller G. An objective definition of a vortex. J Fluid Mech 2005;525:1–26.
[14] Hardalupas YY, Horender S. Phase Doppler anemometer for instantaneous measurements of droplet concentration. In: Proceedings of the 10th international symposium on application of laser techniques to fluid mechanics. Lisboa, Portugal; 2000. p. 23.1.1–13.

[15] Holmen J, Hughes TJR, Oberai AA, Wells GN. Sensitivity of the scale partition for variational multiscale large–eddy simulation of channel flow. Phys Fluids 2004;16:824–7.
[16] Hughes TJR, Oberai AA, Mazzei L. Large eddy simulation of turbulent channel flows by the variational multiscale method. Phys Fluids 2001;13:1784–99.
[17] Hulburt HM, Katz S. Some problems in particle technology – a statistical mechanical formulation. Chem Eng Sci 1964;19:555–74.
[18] John V. Higher order finite element methods and multigrid solvers in a benchmark problem for the 3D Navier–Stokes equations. Int J Num Meth Fluids 2002;40:775–98.
[19] John V. Slip with friction and penetration with resistance boundary conditions for the Navier–Stokes equations – numerical tests and aspects of the implementation. J Comp Appl Math 2002;147:287–300.
[20] John V. Reference values for drag and lift of a two–dimensional time dependent flow around a cylinder. Int J Numer Meth Fluids 2004;44:777–88.
[21] John V. On the efficiency of linearization schemes and coupled multigrid methods in the simulation of a 3d flow around a cylinder. Int J Num Meth Fluids 2006;50:845–62.
[22] John V, Kaya S. A finite element variational multiscale method for the Navier–Stokes equations. SIAM J Sci Comp 2005;26:1485–503.
[23] John V, Kindl A. Numerical studies of finite element variational multiscale methods for turbulent flow simulations. Comput Methods Appl Mech Eng 2010;199:841–52.
[24] John V, Kindl A. A variational multiscale method for turbulent flow simulation with adaptive large scale space. J Comput Phys 2010;229:301–12.
[25] John V, Matthies G. MooNMD – a program package based on mapped finite element methods. Comput Visual Sci 2004;6:163–70.
[26] John V, Matthies G, Rang J. A comparison of time–discretization/linearization approaches for the time–dependent incompressible Navier–Stokes equations. Comput Methods Appl Mech Eng 2006;195:5995–6010.
[27] John V, Novo J. On (essentially) non-oscillatory discretizations of evolutionary convection-diffusion equations. J Comput Phys 2012;231:1570–86.
[28] John V, Roland M. Simulations of the turbulent channel flow at $Re_\tau = 180$ with projection–based finite element variational multiscale methods. Int J Numer Meth Fluids 2007;55:407–29.
[29] John V, Roland M. On the impact of the scheme for solving the higher dimensional equation in coupled population balance systems. Int J Numer Meth Eng 2010;82:1450–74.
[30] John V, Roland M. Simulations of 3d/4d precipitation processes in a turbulent flow field. In: Kreiss G et al., editors. Numerical mathematics and advanced applications. Springer; 2009. p. 479–87.
[31] Kampe HJ. Visibility and liquid water content in clouds in the free atmosphere. J Atmosph Sci 1950;7(1):54–7.
[32] Klein M, Sadiki A, Janicka J. A digital filter based generation of inflow data for spatially developing direct numerical of large eddy simulations. J Comput Phys 2003;186:652–65.
[33] Marchisio DL, Fox RO. Solution of population balance equations using the direct quadrature method of moments. J Aero Sci 2005;36:43–73.
[34] McGraw R. Description of aerosol dynamics by the quadrature method of moments. Aerosol Sci Technol 1997;27:255–65.
[35] Mersmann A. Crystallization technology handbook. 2nd ed. New York: Marcel Dekker Inc.; 2001.
[36] Pruppacher HR, Klett JD. Microphysics of clouds and precipitation. Kluwer Academic Publishers; 1997.
[37] Ramakrishnan S, Collis SS. Turbulence control simulation using the variational multiscale method. AIAA J 2004;42:745–53.
[38] Reeks MW, Fabbro L, Soldati A. In search of random uncorrelated particle motion (RUM) in a simple random flow field. In: ASME 2nd joint US-European fluids engineering summer meeting (FEDSM2006), vol. 1; 2006.
[39] Rogers RR, Yau MK. Cloud physics. 3rd ed. Butterworth–Heinemann; 1989.
[40] Roisman IV, Tropea C. Drops distribution and flux measurements in sprays using the phase Doppler technique. In: 10th international symposium on applications of laser techniques to fluid mechanics; 2000. p. 23/1–23/12
[41] Roisman IV, Tropea C. Flux measurements in sprays using phase Doppler techniques. Atomiz Sprays 2001;11(6):667–700.
[42] Saad Y. Iterative methods for sparse linear systems. 2nd ed. Philadelphia: SIAM; 2003.
[43] Smagorinsky JS. General circulation experiments with the primitive equations. Mon Weather Rev 1963;91:99–164.
[44] Sommerfeld M, Qiu HH. Particle concentration measurements by phase – Doppler anemometry in complex dispersed two-phase flows. Exp Fluids 1995;18(3):187–98.
[45] Vanka S. Block-implicit multigrid calculation of two-dimensional recirculating flows. Comput Meth Appl Mech Eng 1986;59(1):29–48.